



Enhancing thermal safety of hydrophobic silica aerogels by incorporating sodium dodecyl sulfate intercalated layered double hydroxides

Zhi Li¹ · Min Hu¹ · Kai Shen¹ · Fang Zhou¹ · Zhenkui Chen² · Xudong Cheng³ · Qiong Liu¹ · Xiaoxu Wu¹

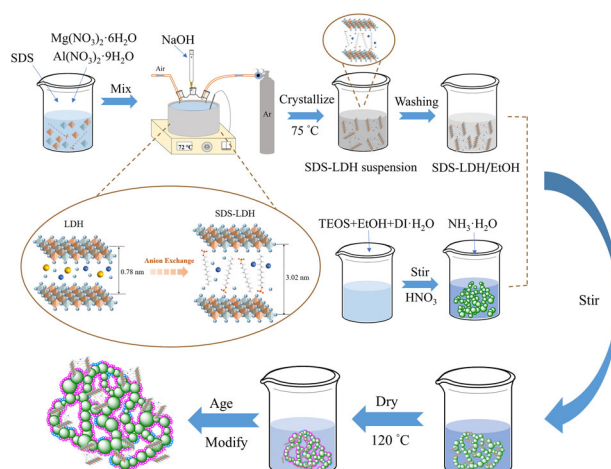
Received: 17 February 2024 / Accepted: 1 April 2024 / Published online: 13 April 2024

© The Author(s), under exclusive licence to Springer Science+Business Media, LLC, part of Springer Nature 2024

Abstract

To enhance the thermal safety and preserve the excellent thermal insulation of hydrophobic silica aerogels (SA), sodium dodecyl sulfate (SDS) intercalated layered double hydroxides (LDH) was incorporated into SA by in situ doping to form SDS-LDH/SA composites. The intercalation modification by SDS extends the layer spacing of LDH and improves the dispersibility of LDH in SA, in favor of the combination between LDH and SA. The physical combination between the SA and SDS-LDH is demonstrated by FTIR analyses. As the content of SDS-LDH rises, the SDS-LDH/SA continues to exhibit a low density (0.11–0.20 g/cm³), low thermal conductivity (<26.8 mW/m/K), and large specific surface area (709.4–839.2 m²/g), ensuring excellent thermal insulation performance. It further finds that the SDS-LDH effectively absorbs heat and inhibits the thermal decomposition of SA. Therein, the onset temperature of thermal decomposition of the SA with 20% SDS-LDH is 114.0 °C higher than that of pure SA. Additionally, it also finds that the gross calorific values of the SDS-LDH/SA decrease with the SDS-LDH content, and all these gross calorific values are lower than that of the pure SA. Hence, SDS intercalated LDH presents significant effects on enhancing the thermal safety of hydrophobic SA without impairing the thermal insulation too much.

Graphical Abstract



✉ Xiaoxu Wu
wuxiaoxu@csu.edu.cn

¹ School of Resource and Safety Engineering, Central South University, Changsha 410083, China

² Department of Engineering Technology and Application, The Army Infantry College of PLA, Nanchang 330103, China

³ State Key Laboratory of Fire Science, University of Science and Technology of China, Hefei 230027, China

Keywords Hydrophobic silica aerogels · Layered double hydroxide · Sodium dodecyl sulfate · Thermal stability · Thermal safety

Highlights

- SDS intercalated LDH was incorporated into SA by in-situ doping to form SDS-LDH/SA composites.
- The intercalation modification by SDS not only increases the interlayer spacing of LDH but also improves the dispersion of LDH in matrix materials.
- The addition of SDS-LDH has no significant effect on the excellent thermal insulation properties of SA and effectively improves the thermal safety of SA.

1 Introduction

Silica aerogels (SA) are novel nano-porous materials with wide-ranging applications in thermal insulation [1, 2], adsorption [3, 4], and energy storage [5, 6]. However, hydrophilic SA is susceptible to water or moisture-affected environments, which can lead to structural collapse due to capillary forces, thus affecting performance and functionality and limiting their applications, therefore, hydrophobicity of SA is usually achieved by introducing stabilizing methylsilyl groups [7]. Nevertheless, when encountering a high temperature during usage, these methylsilyl groups decompose and release flammable volatiles [8], which not only results in loss of hydrophobicity [9] but also induces potential thermal hazard risk [8]. To tackle this issue, hydroxides [10, 11], layered double hydroxides (LDH) [12, 13] and graphene derivatives [14, 15] have been utilized to augment the thermal safety of hydrophobic SA.

Therein, LDH refers to two-dimensional layered nano-materials comprising multiple positively charged layers with intercalated anions situated between them [16], which can be used as catalysis [17], drug carrier [18], CO₂ sequestration [19], environmental remediation [20], flame retardant [21], etc. Besides, LDH mainly exist as minerals in nature, implying that LDH are relatively inexpensive to acquire. Due to the nano-layered structure, halogen-free, and low-cost properties, LDH have been considered as one kind of economic and environmental inorganic nano flame retardants [22]. However, the small layer spacing (0.78 nm) and poor dispersity influence the combination between LDH and matrix materials, which impair the flame retardancy of LDH to some extent [23].

Actually, before being added to matrix materials, LDH are usually modified or functionalized, including intercalation [24], exfoliation [25], reconstruction [26], etc. Therein, intercalation modification of LDH is achieved by inserting polymer molecular chains into the layers of LDH. Through intercalation of LDH, the strong hydrophilicity of layers is weakened, enhancing the compatibility between LDH and matrix materials, which benefits exerting the flame

retardancy of LDH [26–28]. For example, Wu et al. improved flame retardancy of polypropylene (PP) using Mg-Al LDH intercalated by lignin sulfonate sodium [29]. Jiang et al. used amino sulfonate anions modified LDH in ethylene-vinyl acetate (EVA) to enhance flame retardancy and thermal stability of EVA [30]. Shen et al. proved that the thermal stability and flame retardancy of PP nano-composites can be improved by using sodium dodecyl sulfate (SDS) intercalated Ca-Mg-Al LDH [31]. Next, we will further discuss the intercalation modification of LDH by SDS. As we know, SDS is a long-chain polymer molecule and is usually used as a surfactant [32]. The intercalation modification by SDS not only increases the interlayer spacing of LDH but also improves the dispersion of LDH in matrix materials. SDS has been proven to be an excellent organic anion for the intercalation modification of LDH [33, 34]. However, there are no report on the application of SDS intercalated LDH to the thermal safety of hydrophobic SA.

In this study, sodium dodecyl sulfate (SDS) intercalated LDH (SDS-LDH) was incorporated into hydrophobic SA (SDS-LDH/SA) to adjust thermal safety. The physico-chemical properties, thermal stability, and combustion properties of SDS-LDH/SA are investigated in detail. This work finally demonstrates that the SDS-LDH has good dispersibility in SA and significantly improves the thermal safety of hydrophobic SA, which expands the practical application of hydrophobic aerogels in the field of thermal insulation.

2 Experimental section

2.1 Raw materials

Tetraethoxysilane (TEOS, 98%), ethanol (EtOH, 99.7%), n-hexane (97.0%), and sodium dodecyl sulfate (SDS, 92.5–100.5%) were purchased from Sinopharm Chemical Reagent Co., Ltd. (Shanghai, China). Nitric acid (HNO₃, 8 M) and ammonia water (NH₃·H₂O, 25–28%) were used as acid and basic catalyst, respectively. Al(NO₃)₃·9H₂O

(99.0%), $\text{Mg}(\text{NO}_3)_2 \cdot 6\text{H}_2\text{O}$ (99.0%), NaOH (96.0%) and Hexamethyldisilazane (HMDZ, 99.0%) used in the experiments were purchased from Aladdin Reagent Co., Ltd (Shanghai, China). Deionized water was generated using an ultra-pure water machine (ECO-S, Hitech, Shanghai, China).

2.2 Preparation

2.2.1 Preparation of SDS-LDH

Utilizing the coprecipitation method, SDS intercalated Mg-Al layered double hydroxides were synthesized. Initially, a three-necked flask was filled with inert gas. Following this, 23 g of $\text{Mg}(\text{NO}_3)_2 \cdot 6\text{H}_2\text{O}$, 11.3 g of $\text{Al}(\text{NO}_3)_3 \cdot 9\text{H}_2\text{O}$, and 17.3 g of SDS were meticulously weighed and dissolved in 300 ml of deionized water. The resulting solution was then transferred into the flask and stirred vigorously at 70°C for 30 min until a homogeneous, clear solution was formed. Simultaneously, a 0.8 mol/l NaOH solution was consistently dripped into the flask, adjusting pH to 11. Subsequent to this, the solution underwent vigorous stirring for 1 h, ensuring a thorough reaction among $\text{Mg}(\text{NO}_3)_2 \cdot 6\text{H}_2\text{O}$, $\text{Al}(\text{NO}_3)_3 \cdot 9\text{H}_2\text{O}$, SDS, and NaOH , leading to the precipitation of SDS intercalated layered double hydroxide (SDS-LDH). The resulting blend underwent crystallization by being placed in a drying oven at 75°C for 24 h, leading to the creation of a milky white turbid liquid. The removal of the supernatant was succeeded by filtration and repeated rinses with distilled water until the pH of the supernatant approached neutrality. Finally, to prepare the SDS-LDH/EtOH emulsion, several iterations of ethanol washing were conducted, ensuring the successful formulation of the SDS-LDH/EtOH emulsion. The concentration of the final SDS-LDH/EtOH emulsion obtained was in the

range of 10–20%, calculated from the mass of SDS-LDH before and after drying.

2.2.2 Preparation of SDS-LDH/SA

The synthesis process depicted in Fig. 1 initiates by mixing 5.75 ml of TEOS, 15 ml of EtOH, 1 ml of deionized water and 0.3 ml of HNO_3 and stirring for 5 min. Subsequently, the mixture undergoes a complete 12-h hydrolysis process in a 45°C water bath. 0.5 ml of $\text{NH}_3 \cdot \text{H}_2\text{O}$ is then added to the hydrolysate, and after 5 min of stirring, various quantities of SDS-LDH/EtOH are incorporated into the silica sol through a combination of mechanical stirring and ultrasonic treatment. These quantities, representing 5%, 10%, 15%, and 20% of the total mass of silica aerogels, are denoted as SDS-LDH/SA-x, with x indicating 5%, 10%, 15%, 20%, respectively. Gelation typically occurs within 30 min. The ensuing SDS-LDH/aerogels are aged in EtOH for 18 h, followed by an exchange with n-hexane for an additional 18 h. Subsequent to this, the aerogels are modified for 48 h with 50 ml of HMDZ/hexane solution in a ratio of 3:22 HMDZ to hexane. Finally, the wet SDS-LDH/aerogels are subjected to drying under ambient pressure at 120°C for 4 h, culminating in the formation of SDS-LDH/SA.

2.3 Methods of characterization

Using a field emission scanning electron microscope (SEM, Sigma 300, ZEISS, Germany), the microstructures were observed. An energy dispersive spectroscopy (EDS, Smartex, ZEISS, Germany) was employed to the composition and content of elements of the SDS-LDH/SA.

For the measurement of N_2 sorption isotherms at 77 K, an automatic surface area and porosity analyzer (Quantachrome, AUTOSORB IQ, USA) was utilized. The specific

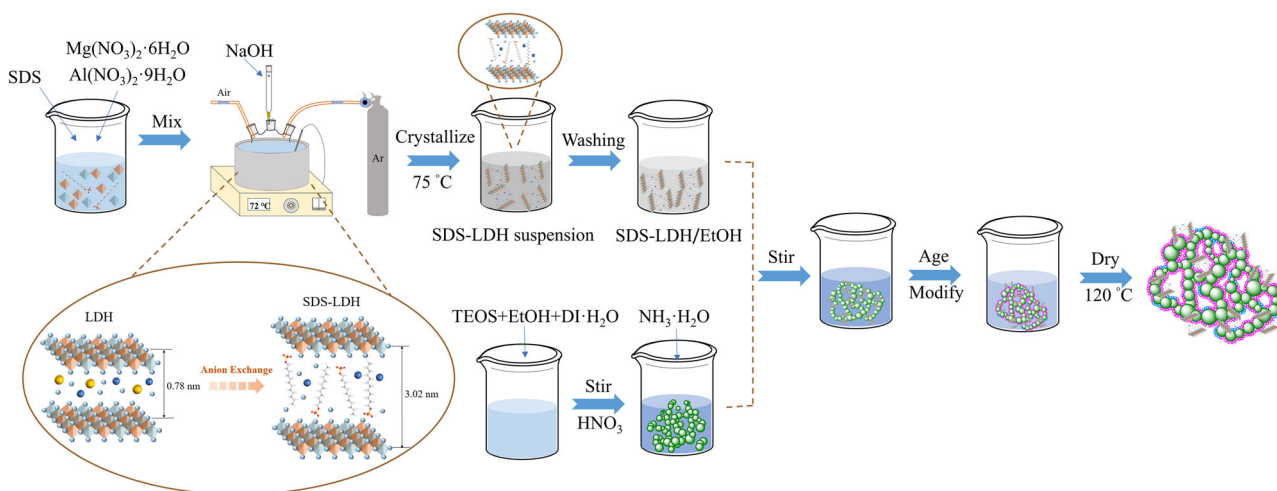


Fig. 1 Schematic diagram for synthesizing SDS-LDH/SA

surface area was calculated using the Brunauer-Emmett-Teller (BET) method [35], while the Barrett-Joyner-Halenda (BJH) method was applied to determine parameters [36]. To provide a more comprehensive analysis of the aerogel's pore structure, assumptions of cylindrical pores were made, and the pore volume (V_{pore}) and the average pore diameter (D_{pore}) were calculated according to the following equations [7]:

$$V_{\text{pore}} = \frac{1}{\rho_t} - \frac{1}{\rho_s} \quad (1)$$

$$D_{\text{pore}} = \frac{4V_{\text{pore}}}{S_{\text{BET}}} \quad (2)$$

Although the calculation of the BET surface area does not directly involve the assumption of pore shape, it provides an efficient and reliable method for evaluating the specific surface area of a material. Therefore, the BET specific surface area (S_{BET}) was used in the calculation of D_{pore} .

A tap density meter (ZS-202, Liaoning Instrument Research Institute, China) was utilized to measure the tap density (ρ_t) under continuous vibration at 300 r/min for 10 min. The porosity was determined using the following method:

$$\text{Porosity} = \left(1 - \frac{\rho_t}{\rho_s}\right) \times 100\% \quad (3)$$

where ρ_s is the skeletal density of SA (about 2.2 g/cm³) [37].

A transient hot wire method was utilized to measure the thermal conductivities using a constant thermal analyzer (TC3000E, XIATECH, China) at room temperature. The samples were ground into powders and placed in a sample box, ensuring complete coverage of the sensor by the samples.

The confirmation of chemical groups and bonds was achieved through the Fourier transform infrared (FTIR, Nicolet 8700, USA). The samples were ground into powder and dispersed uniformly on the test platform, and the contact angle was measured by dropping 5 μl of water on the sample surface using an automatic contact angle measuring

instrument (ASR-705S, Guangdong Aisry Instrument Technology Co., Ltd, China).

The crystal phase of the specimens was determined using X-ray diffraction (XRD, D8 Advance, Bruker, USA). The interlayer spacing of LDH was calculated based on Bragg's equation as follows:

$$d_{(003)} = \frac{n\lambda}{2 \sin \theta} \quad (4)$$

where θ represents the angle between the incident X-ray and the corresponding crystal plane, n signifies the diffraction order, and λ denotes the wavelength of X-ray (The Cu target wavelength used for the test was 1.5418 Å).

The thermal stability analysis was tested using thermogravimetry-differential scanning calorimetry (TG-DSC, SDT Q650, TA Instrument, USA). The tests were carried out in air, covering a temperature range from room temperature to 800 °C, and a heating rate of 10 °C/min.

For the measurement of gross calorific value (GCV), an oxygen bomb calorimeter (AM-C1009, Changsha Yuanfa Instrument Co., Ltd, China) was employed in accordance with ISO 1716:2018.

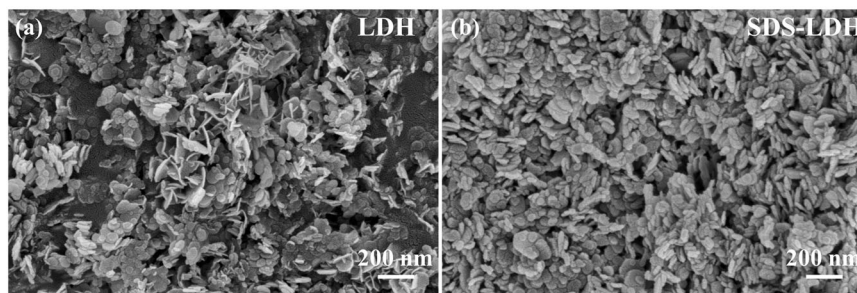
3 Results and discussion

3.1 Basic characterization of SDS-LDH

In Fig. 2a, the microstructures of LDH present a distinct lamellar structure. The strong electrostatic interaction between the layers [38] results in the aggregation of a considerable number of LDH particles. In Fig. 2b, the SDS-LDH still maintains a layered structure. Notably, the layer thickness of the SDS-LDH increases significantly. Notably, the particle aggregation of SDS-LDH is weakened and the particle distribution becomes more uniform compared to that of LDH.

In Fig. 3a, the XRD pattern of the LDH displays characteristic diffraction peaks at 11.34°, 22.75°, 34.40°, 38.50°, 45.45°, 60.35°, and 61.62°, corresponding to the reflections of (003), (006), (012), (015), (018), (110), and (113) planes, respectively. These peaks indicate the

Fig. 2 Microstructures of the LDH (a) and SDS-LDH (b)



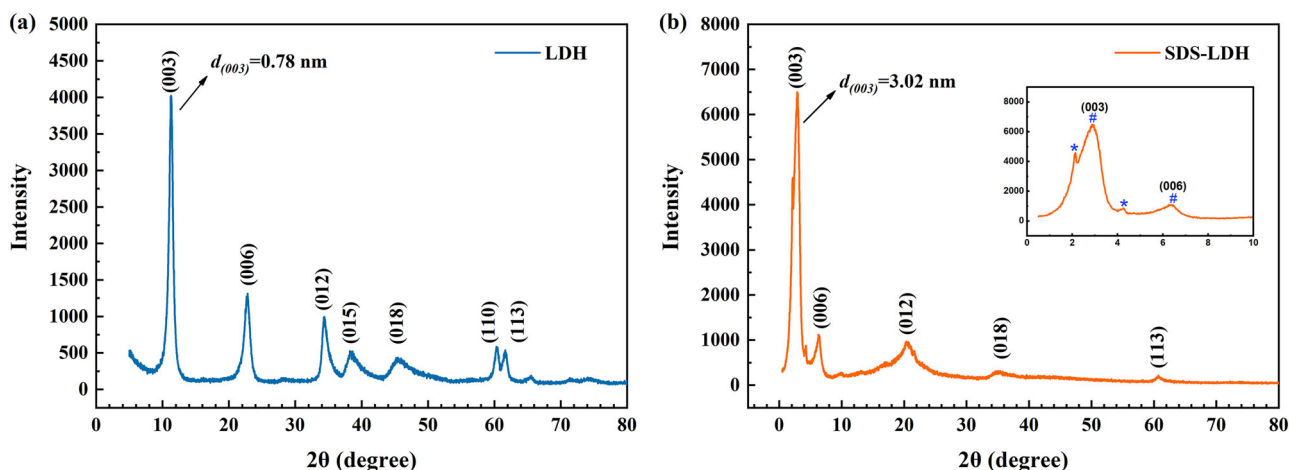


Fig. 3 XRD patterns of LDH (a) and SDS-LDH (b)

Table 1 The layer spacings of the LDH and SDS-LDH

Samples	(003)		Height of layer spacing (nm)
	2θ (°)	d (nm)	
LDH	11.34	0.78	0.30
SDS-LDH	2.93	3.02	2.54

presence of a typical hydroxyl structure, keeping consistent with the reference [39, 40].

The XRD pattern of the SDS-LDH reveals the retention of a layered structure akin to hydroxyl, which indicates that the intercalation modification does not disrupt the integrity of the crystalline and layered structure of LDH. In addition, two laminar structures (labeled with * and #) are formed when SDS intercalates LDH, and the intensity of the diffraction peak labeled with * decreases with increasing concentration of SDS until it disappears [41, 42]. In Fig. 3b, the two small peaks near the (003) peak of SDS-LDH may be due to the insufficient concentration of SDS, so the diffraction peak labeled with * can still be observed. A comparison between SDS-LDH and LDH reveals noticeable shifts in the (003), (006), and (012) diffraction peaks of SDS-LDH toward lower angles. As indicated in prior study [43], a decrease in the (003) diffraction peak angle indicates an increase in the layer spacing. Thus, the intercalation of SDS leads to an expansion of the layer spacing of the LDH.

The $d_{(003)}$ represents the sum of the length of the interlayer anions along the long axis and the thickness of the layered double hydroxide laminates. As depicted in Table 1, the LDH exhibits a layer spacing of $d_{(003)}$ at 0.78 nm, a layer thickness of 0.48 nm [44], and the layer height of 0.3 nm. The layer spacing $d_{(003)}$ of the SDS-LDH is 3.02 nm, along with an interlayer height is 2.54 nm. Notably, this interlayer height surpasses the length of the

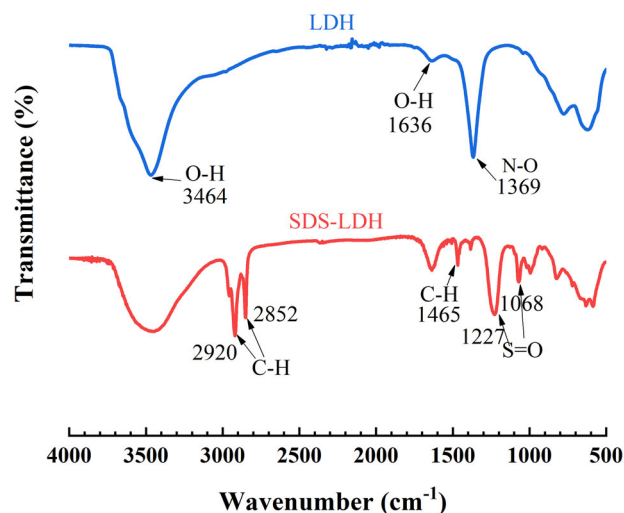


Fig. 4 FTIR spectra of the LDH and SDS-LDH

dodecyl sulfate anion (DS^-) in SDS, which is 1.99 nm [45]. This discrepancy can be attributed to the presence of a small quantity of water molecules in the actual structure, leading to an augmentation of the interlayer height. Hence, it acquires that the long chain DS^- is vertically interspersed between the LDH layers and significantly increases the layer spacing.

The FTIR spectra of the LDH and SDS-LDH have been compared in Fig. 4. For the LDH, the characteristic absorption band in the range of 3200–3700 cm^{-1} corresponds to the stretching vibrations of hydroxyl groups on the LDH layers [46]. The absorption peak at 1636 cm^{-1} indicates the bending vibration of water molecules ($\delta-OH$) between the LDH layers [47]. The absorption peak at 1369 cm^{-1} is attributed to the stretching vibration of the N–O bond from the interlayer anions, NO_3^- [39]. For the SDS-LDH, the vibration peaks located at 2920 cm^{-1} and

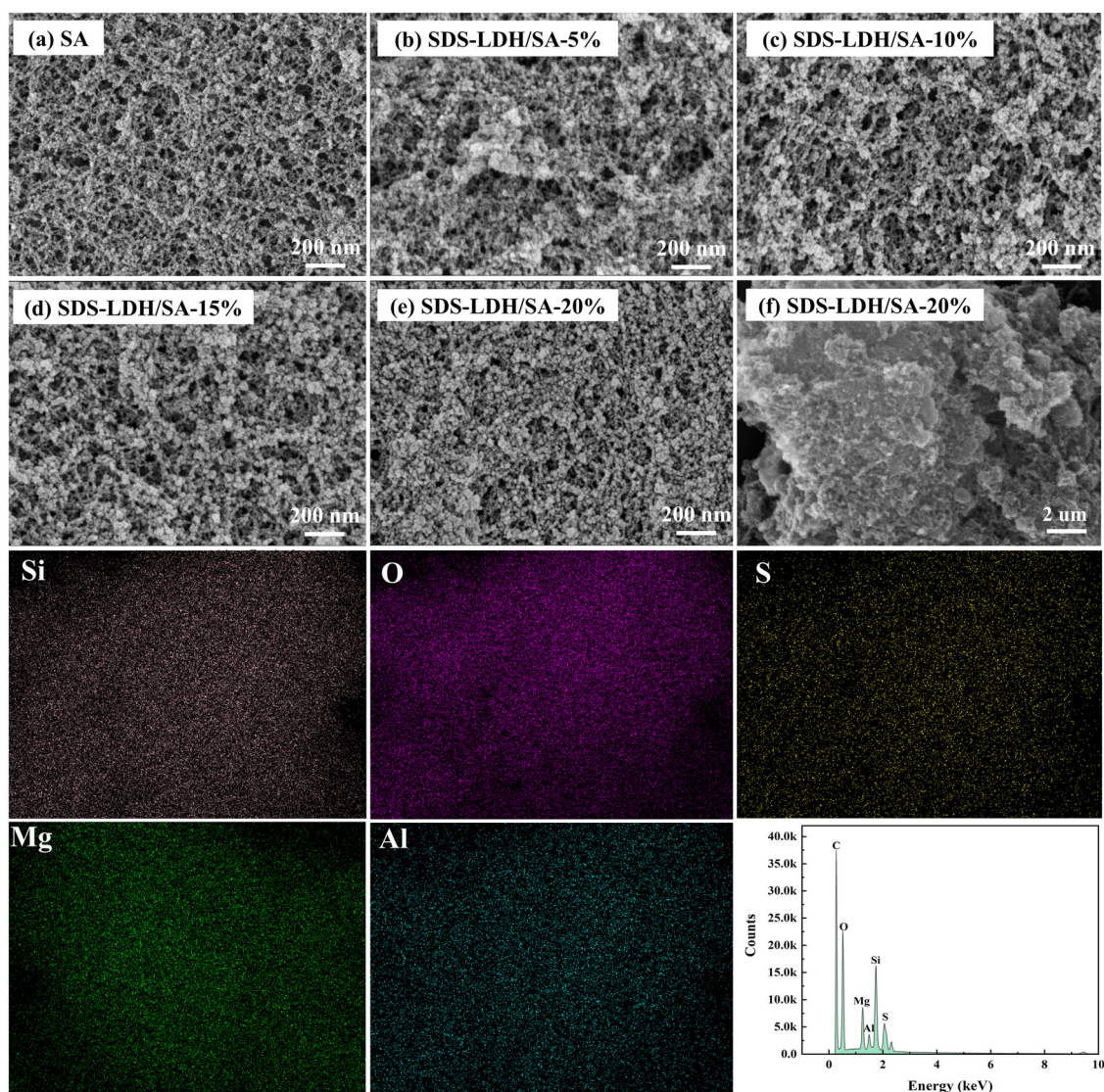


Fig. 5 Microstructures of SA (a), SDS-LDH/SA (b–f), and element distributions of the SDS-LDH/SA-20%

2852 cm^{-1} correspond to the asymmetric and symmetric stretching vibrations of C–H bonds in the alkyl group [48], respectively. The absorption peak at 1465 cm^{-1} represents the bending vibration of $-\text{CH}_2$ groups in SDS [49]. Additionally, the antisymmetric and symmetric stretching vibration peaks of S=O are observed at 1227 cm^{-1} and 1068 cm^{-1} [50, 51]. These vibration peaks confirm the presence of SDS in the LDH. Moreover, the intensity of the N–O stretching vibration peak is significantly reduced compared to LDH. This implies that a significant portion of NO_3^- anions within the LDH layers has been substituted with DS^- anions. Combining the FTIR and XRD analyses confirms that the DS^- anions have been effectively embedded into the layers of the LDH by ion exchange method while retaining the original layered structure.

3.2 Basic characterization of SDS-LDH/SA

Figure 5 displays the microstructures of the SA, LDH/SA, and SDS-LDH/SA, all of which exhibit three-dimensional nano-network structures. From the SEM images, it is not easy to compare the relative pore size of the SDS-LDH/SA and the pure SA. However, in the case of the SDS-LDH/SA, their pore sizes decrease with the SDS-LDH content increasing.

For a more in-depth examination of the distribution of the SDS-LDH in the SDS-LDH/SA, the element distributions are illustrated in Fig. 5. The EDS spectra reveal a uniform distribution of Si, Mg, Al, S, and O elements, with overlapping distribution regions for these five elements. This result confirms the successful integration of SDS-LDH into the SDS-LDH/SA. Additionally, it implies the

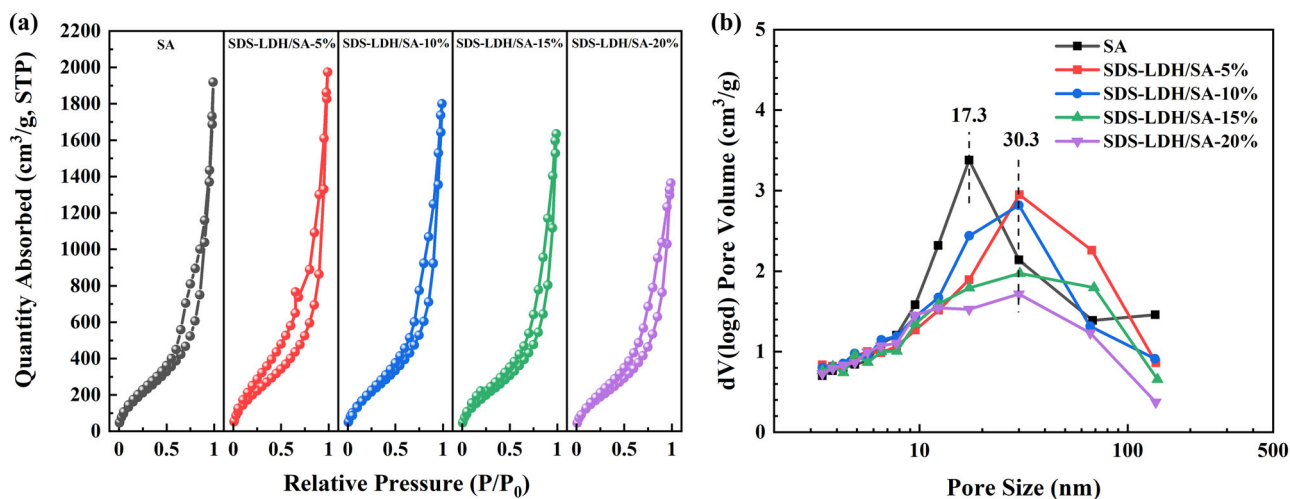


Fig. 6 N_2 sorption isotherms (a) and pore size distribution (b) of SA and SDS-LDH/SA

Table 2 Pore parameters of the pure SA and SDS-LDH/SA

Samples	BET surface area (m^2/g)	Pore volume ^a (cm^3/g)	Average pore size ^b (nm)	V_{pore} ^c (cm^3/g)	D_{pore} ^d (nm)
SA	903.7	2.8	12.2	8.5	37.7
SDS-LDH/SA-5%	839.2	3.1	14.5	6.9	33.1
SDS-LDH/SA-10%	814.2	2.8	13.7	6.5	31.9
SDS-LDH/SA-15%	747.5	2.5	13.5	5.6	29.9
SDS-LDH/SA-20%	709.4	2.2	11.9	4.6	26.0

^{a,b}The pore volume and average pore size were determined using the BJH method from N_2 desorption data. Uncertainties: BET surface area $\sim 50 m^2/g$; pore volume and average pore diameter with a relative fluctuation of 5% [66]

^{c,d}The V_{pore} and D_{pore} were calculated following Eqs. (1) and (2) with 10% relative uncertainty [67]

simultaneous presence of silica skeletons alongside nanosheets derived from SDS-LDH, even though their identification may pose challenges.

To delve deeper into the pore structure, N_2 sorption isotherms were employed. As illustrated in Fig. 6a, the N_2 sorption isotherms of SA and SDS-LDH/SA exhibit striking similarities. And their curves prove that they are mesoporous material [52]. The most difference lies in the change of the maximum absorbed quantity, namely, the maximum absorbed quantity of the SDS-LDH/SA decreases with the SDS-LDH content. In this regard, the introduction of SDS-LDH does not notably alter the mesoporous characteristics of the SDS-LDH/SA. In Fig. 6b, the SA has a relatively concentrated pore size distribution (PSD) ranging between 20–60 nm and the most probable pore size of 17.3 nm, while the SDS-LDH/SA have a wider PSD ranging between 10–100 nm and the most probable pore size of 30.3 nm. Compared with the SA, the SDS-LDH/SA consists of mesopores and more macropores. To summarize above analyses, the introduction of SDS-LDH mainly affect the pore size distribution of the SDS-LDH/SA without changing the mesoporous property.

Table 2 lists the detailed pore parameters. The specific surface areas of all the SDS-LDH/SA are lower than that of the SA ($903.7 m^2/g$). With the SDS-LDH content increasing within 5–20%, the specific surface areas of the SDS-LDH/SA decrease from $839.2 m^2/g$ to $709.4 m^2/g$, the pore volumes decrease from $3.1 cm^3/g$ to $2.2 cm^3/g$, and the average pore sizes decrease from 14.5 nm to 11.9 nm. All these variations are caused by the introduction of SDS-LDH, which influences the porous skeleton structures, as shown in Fig. 5. Besides, in comparison with LDH/SA [12], the SDS-LDH/SA have a relatively smaller pore parameters.

In addition, the calculated values of V_{pore} and D_{pore} appear to be higher than the experimental values. This discrepancy indicates the potential presence of macropores beyond the scope of the nitrogen sorption test's characterization range and the potential distortion of the silica aerogel during nitrogen sorption measurements [7].

Figure 7a illustrates the influence of the SDS-LDH content on the density and porosity of SA. As the SDS-LDH content rises, the density of the SDS-LDH/SA increases from $0.11 g/cm^3$ to $0.20 g/cm^3$. The observed trend in this

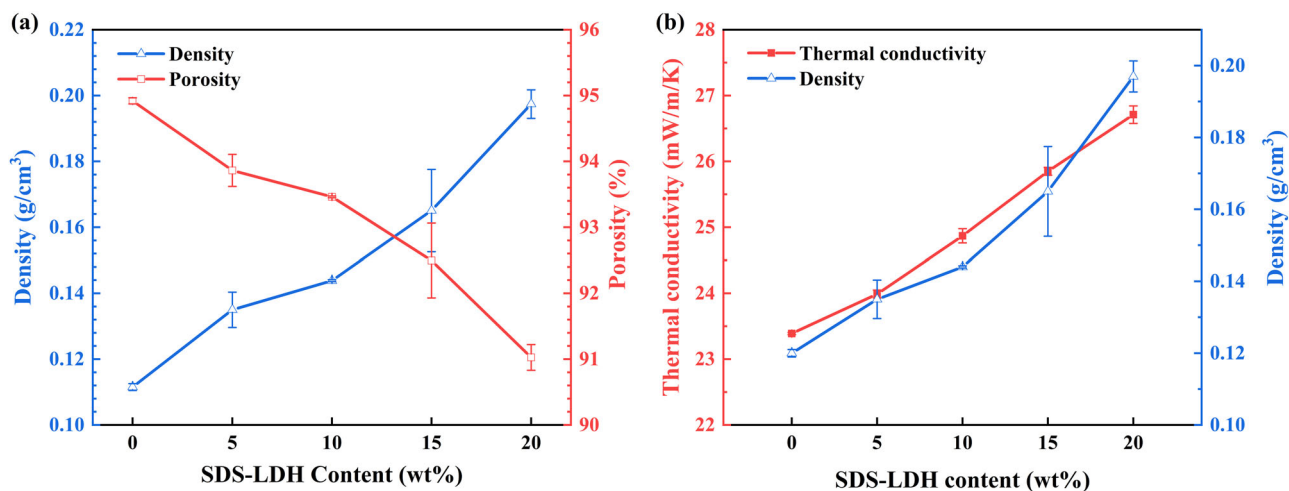


Fig. 7 Density and porosity (a) and thermal conductivity (b) of the SDS-LDH/SA

change is linked to the larger density of the SDS-LDH, compared to SA. The porosity of the SDS-LDH/SA has an opposite tendency, i.e., decreasing from 93.9% to 91.0%. In spite of that, the SDS-LDH/SA still maintain a high level of porosity.

In Fig. 7b, the thermal conductivity of the SDS-LDH/SA increases from 23.9 mW/m/K to 26.8 mW/m/K as the doping amount of SDS-LDH increases, which is higher than LDH/SA [12]. This phenomenon can be ascribed to the incorporation of SDS-LDH, which creates additional heat transfer channels. As a result, the three-dimensional porous skeleton of the silica aerogel is no longer the sole medium for heat transfer, leading to an increase in solid-phase heat conduction capacity. Regarding gas-phase heat conduction, the change in heat transfer caused by variations in pore size is negligible. Overall, the incorporation of SDS-LDH enhances the thermal conductivity of the SDS-LDH/SA. Note that, at a doping amount of 20%, the thermal conductivity of the SDS-LDH/SA is slightly higher than that of static air (26 mW/m/K). Therefore, when the SDS-LDH doping content does not exceed 20%, the prepared SDS-LDH/SA can maintain a low thermal conductivity.

Figure 8 shows the infrared spectrum of SDS-LDH/SA. The broad absorption peaks around 1650 cm^{-1} and 3440 cm^{-1} are attributed to the asymmetric stretching and bending vibrations of the -OH group, respectively [53, 54]. The symmetric and asymmetric tensile vibration peaks of the C-H bond of -CH₃ group were observed near 2980–2880 cm^{-1} [55]. Meanwhile, the peaks at 2920 cm^{-1} and 2852 cm^{-1} coincide with the anti-symmetric and symmetric -CH₂- stretching modes [40]. The characteristic peaks of 1255 cm^{-1} , 846 cm^{-1} , and 759 cm^{-1} belong to the Si-C bond [56], indicating that the surface modification has successfully introduced Si-(CH₃)₃ group, which is a hydrophobic chemical group [57]. This group makes SDS-LDH/SA composites exhibit good resistance to water and

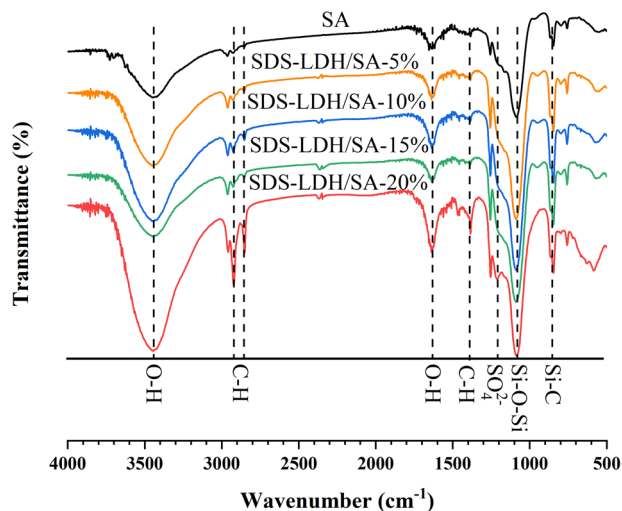


Fig. 8 FTIR spectra for SDS-LDH/SA

moisture. In addition, the absorption peak at 1085 cm^{-1} corresponds to the symmetric tensile vibration mode of the Si-O-Si bond [58]. The asymmetric stretching absorption peak of SO_4^{2-} was observed at 1120 cm^{-1} , which is a characteristic peak of SDS anion [59]. With the increase of SDS-LDH doping content, the absorption peak intensity of SO_4^{2-} was continuously enhanced. Nevertheless, upon comparison with the FTIR spectra of SA and SDS-LDH, the absence of new chemical bonds indicates that the formation of SDS-LDH/SA is a result of the physical combination of SA and SDS-LDH.

Figure 9 shows the contact angle of SDS-LDH/SA with SDS-LDH content ranging from 5 to 20%. The contact angle (131.8°–140.6°) of SDS-LDH/SA is slightly smaller than that of SA (142.6°) and LDH/SA (137.7°–141.7°) [12]. The decrease in contact angle is believed to be related to the hydrophilic head groups of SDS [51]. The hydrophobicity of SDS-LDH/SA diminishes with the escalating SDS-LDH

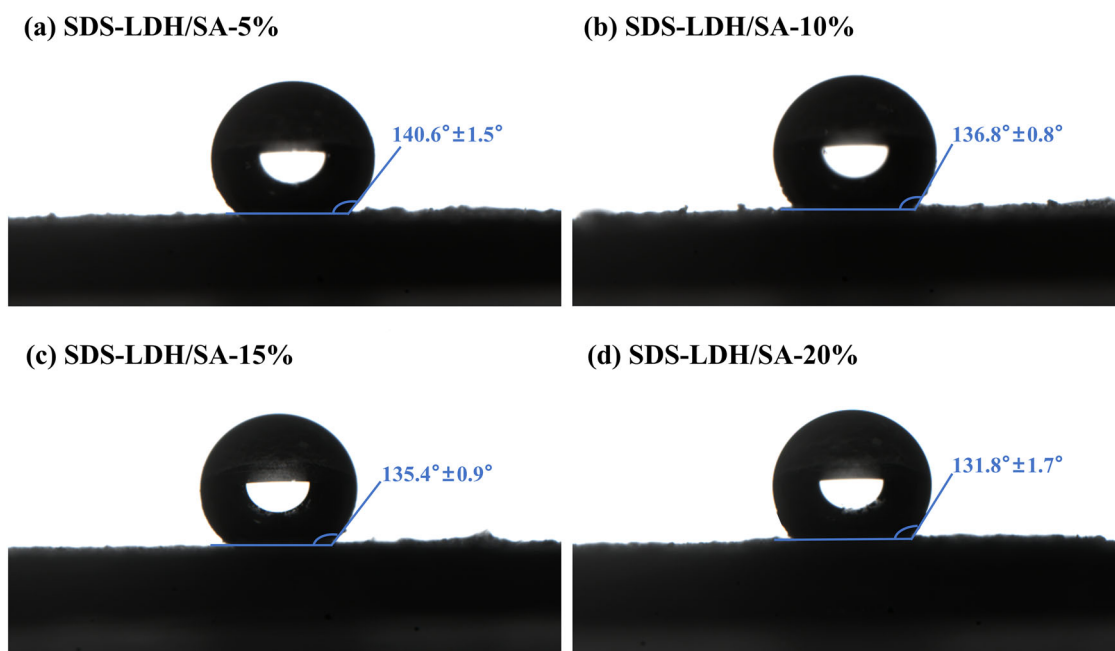


Fig. 9 Contact angles of SDS-LDH/SA with different mass fraction of SDS-LDH (a) 5%; (b) 10%; (c) 15%; (d) 20%

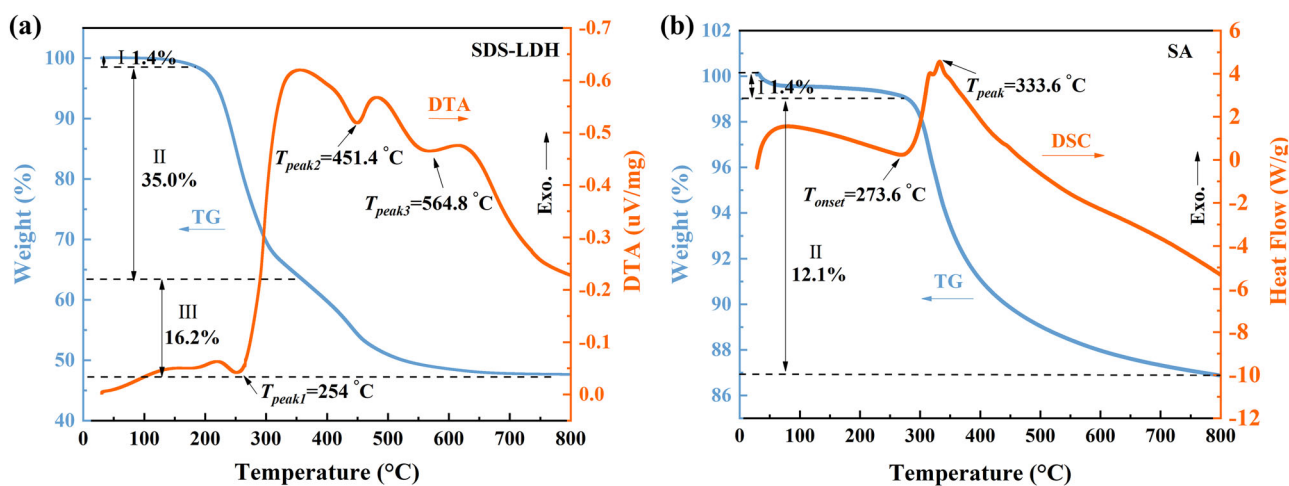


Fig. 10 TG curves of SDS-LDH (a) and SA (b)

doping amount. Nevertheless, all samples had contact angles greater than 130° and showed good hydrophobicity. In other words, the introduction of SDS-LDH has no significant damage to the hydrophobicity of SDS-LDH/SA. This indicates that SDS-LDH/SA can still meet the requirements of hydrophobic.

3.3 Thermal stability

Figure 10a illustrates the TG-DTA curve of SDS-LDH. The decomposition process of SDS-LDH undergoes three distinct stages. In the first stage ($<170^\circ\text{C}$), the primary process entails the elimination of physically adsorbed surface water

molecules and interlayer structural water [60], resulting in a mass loss of $\sim 1.4\%$ of the total mass. During the second stage ($170\text{--}380^\circ\text{C}$), the reactions occurring in SDS-LDH differ from those in LDH. This stage includes not only the dehydroxylation of SDS-LDH layers, leading to the release of a significant amount of water but also the decomposition of SDS alkyl chains [60]. Consequently, this stage exhibits a relatively large weight loss, accounting for $\sim 35\%$ of the total mass. The maximum weight loss peak is observed at around 254°C . In the third stage ($>380^\circ\text{C}$), the weight loss is primarily caused by the decomposition of decomposition of SDS sulfate [61], accounting for $\sim 16.2\%$ of the total mass loss.

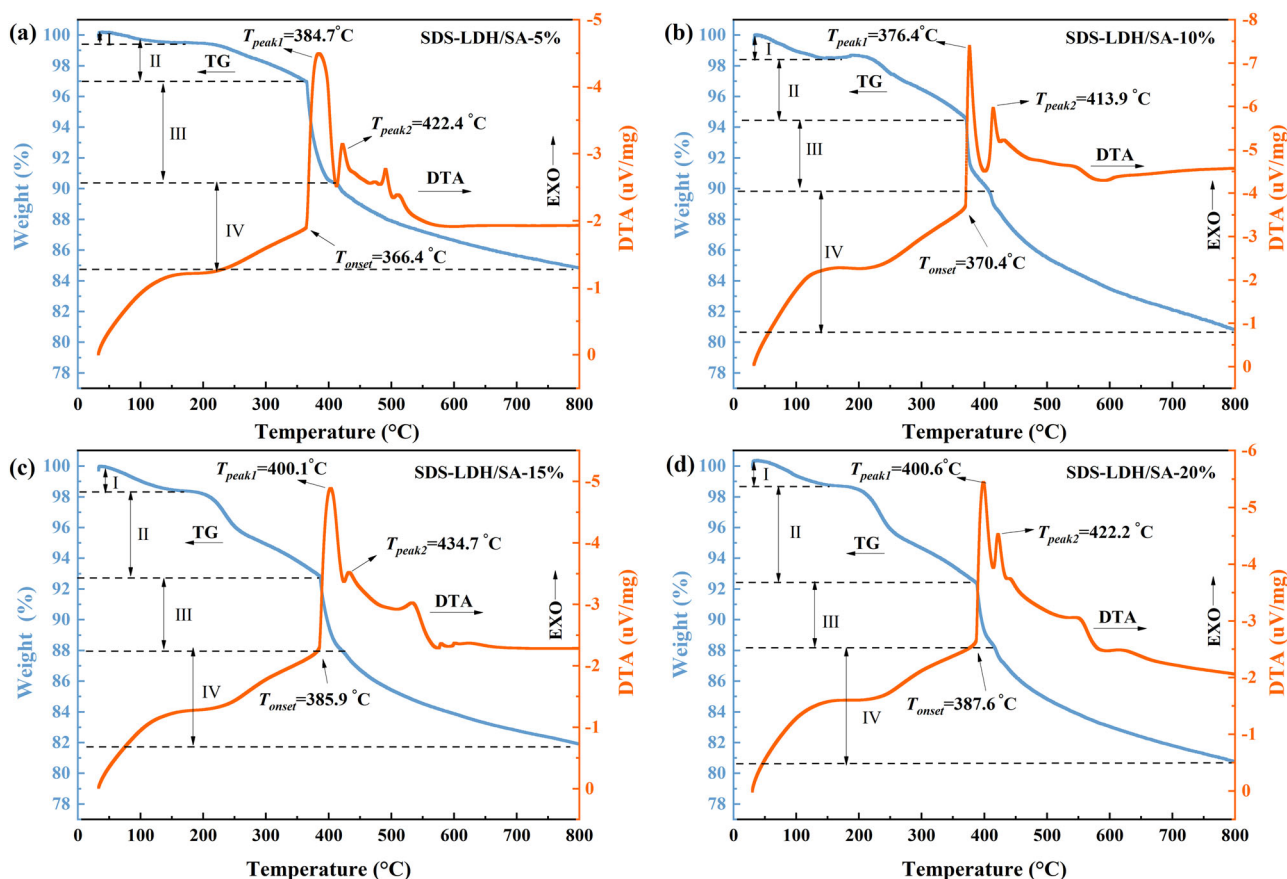


Fig. 11 TG-DTA curves of SDS-LDH/SA with different mass fraction of SDS-LDH (a) 5%; (b) 10%; (c) 15%; (d) 20%

From the DTA curve, it is difficult to determine whether SDS-LDH is an exothermic or an adsorptive reaction because the DTA curve suffers from baseline unevenness, but combined with the DTA curve of LDH [12] and the analysis of previous studies [62], it can be judged that there are three adsorptive peaks in Fig. 10a. The first endothermic peak appears at 254 °C. We believe that the endothermic peak is caused by dehydroxylation on the lamellar, and dehydration between the hydroxyl groups occurs, which is an endothermic reaction. Compared with LDH, the dehydroxylation temperature is lower than LDH, because SDS insertion between LDH layers reduces the hydrogen bonding between the hydroxyl groups on LDH layers, leading to the dehydration and decomposition of some hydroxyl groups at low temperature. This is consistent with previous reports on SDS intercalation LDH [62, 63]. However, the thermal decomposition of SDS also occurred in this process, and a second endothermic peak appeared at 451 °C with increasing temperature. At this stage, interlayer water molecules are removed and interlayer anion DS⁻ is decomposed [61]. It can be seen from the DTA curve that there is an insignificant endothermic peak at 564.8 °C. Due to the imbalance of laminates, LDH decomposes and the laminates

collapse [64]. The dehydroxylation of LDH is advanced, but it may be endothermic due to the thermal decomposition of SDS, thus contributing to cooling [65]. The decomposition temperature of SDS-LDH layered structure is delayed by about 65 °C [12].

Figure 10b depicts the TG-DSC profiles of SA, a subject thoroughly examined in our earlier study [12]. The TG-DTA curves of SDS-LDH/SA are shown in Fig. 11. The complete process of thermal decomposition is considered to result from the combined effects of the thermal oxidation of SA and SDS-LDH. The exothermic reaction of thermal oxidation in Si-CH₃ is counterbalanced by the endothermic nature of SDS-LDH thermal decomposition. As a result, the energy released during the thermal oxidation of Si-CH₃ compensates for the energy consumed in the thermal decomposition of SDS-LDH. Taking these factors into account, it is proposed that the broad exothermic peak of Si-CH₃ is segmented into three relatively narrow exothermic peaks due to the intricate energy dynamics between the two reactions.

The onset decomposition temperature (T_{onset}) and peak decomposition temperature (T_{peak}) of the thermal decomposition reaction of the material are important parameters reflecting its thermal stability. In Fig. 12a, the

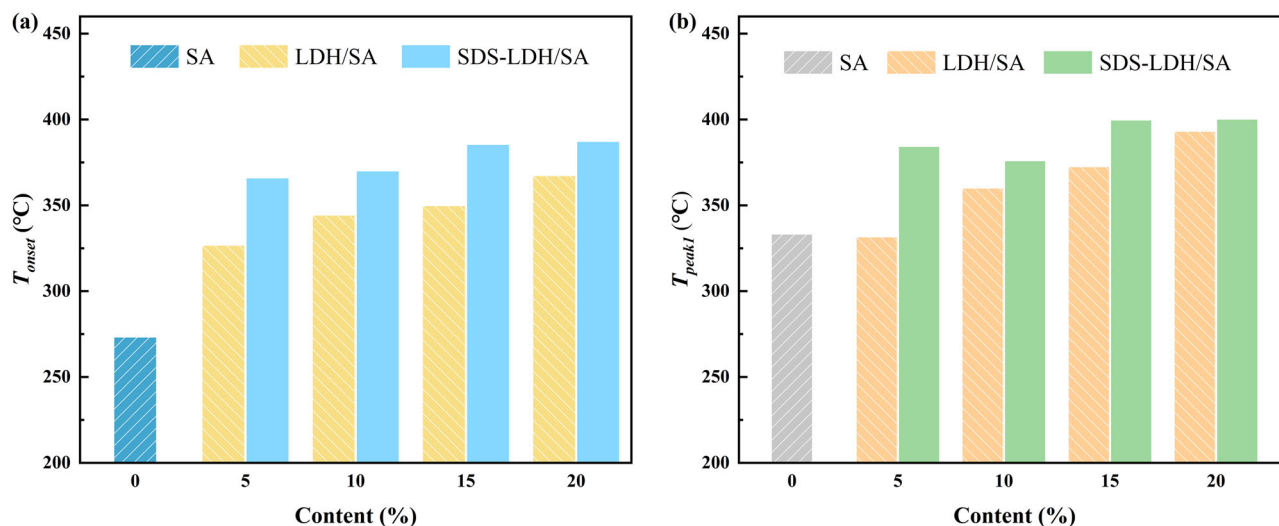


Fig. 12 The T_{onset} (a) and T_{peak1} (b) data of pure SA, LDH/SA and SDS-LDH/SA

T_{onset} and T_{peak} of Si-CH₃ of pure SA are 273.6 °C and 333.6 °C, respectively. While the thermal oxidation and decomposition reaction of the Si-CH₃ groups in SDS-LDH/SA materials are delayed. Furthermore, with an increase in SDS-LDH content, the T_{onset} of SDS-LDH/SA increases from 366.4 °C to 387.6 °C, compared with SA, an increase of 114 °C. And the T_{peak1} of SDS-LDH/SA increases from 384.7 °C to 400.6 °C, compared with SA, which increased by 67 °C. The thermal decomposition temperature of Si-CH₃ is extended due to a large amount of heat absorbed by the decomposition reaction of SDS-LDH, which prolongs the time that the aerogel maintains hydrophobicity to a certain extent and improves the heat insulation application of hydrophobic silica aerogel. In the course of the thermal decomposition process of SDS-LDH, a substantial quantity of energy is absorbed through the dehydroxylation of SDS-LDH layers and the vaporization of adsorbed water and interlayer structural water. Furthermore, the resulting metal oxide, such as MgO, acts as a high-temperature barrier material, proficiently impeding heat transfer. These factors collectively contribute to the postponed thermal decomposition of SDS-LDH/SA, ultimately augmenting their thermal stability.

It is worth noting that the T_{onset} and T_{peak1} of SDS-LDH/SA are higher than that of LDH/SA. As shown in Fig. 12, taking 5% doping amount as an example, the T_{onset} of LDH/SA-5% is 327.2 °C, while the T_{onset} of SDS-LDH/SA-5% is 366.4 °C, an increase of 39.2 °C. It was found that this is mainly attributed to the heat absorption during the thermal decomposition of SDS in stage II, which leads to a decrease in the surrounding temperature and consequently delays the decomposition of Si-CH₃. This finding indicates that the incorporation of SDS intercalated LDH is more effective in improving the thermal stability of SDS-LDH/SA.

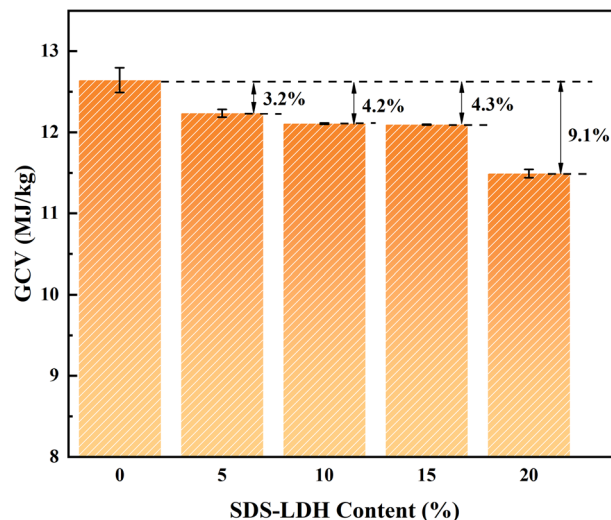


Fig. 13 GCV of the SDS-LDH/SA

3.4 Gross calorific value

The gross calorific value (GCV) is a critical indicator for evaluating the thermal safety of aerogels. Figure 13 presents the total calorific value of SA and SDS-LDH/SA. SA exhibits a GCV of 12.6 MJ/kg, indicating a high thermal hazard. With the introduction of SDS-LDH doping content, the GCV of SDS-LDH/SA diminishes from 12.2 MJ/kg to 11.5 MJ/kg, with the addition of 20% SDS-LDH, the GCV undergoes a reduction of 9.1%, indicating that the integration of SDS-LDH proves effective in lowering the combustion calorific value of SA. However, the combustion calorific value of SDS-LDH/SA is reduced less than that of LDH/SA [12]. This can be attributed to the higher organic group content present in SDS itself.

4 Conclusions

To enhance the compatibility between LDH and hydrophobic silica aerogels (SA), the intercalation modification of LDH was carried out by using SDS. The modified SDS-LDH was incorporated into SA to form the SDS-LDH/SA composites and the physicochemical properties and thermal safety were investigated in detail. Intercalation by SDS expanded the interlayer spacing of LDH, and enhanced the dispersibility of LDHs in SA, both of which benefited to the better compatibility between the SDS-LDH and SA. The incorporation of SDS-LDH had no significant impact on the three-dimensional nanoporous structures of SA and the excellent thermal insulation of SA was retained. It found the SDS-LDH effectively suppressed the thermal decomposition of SA by absorbing heat and physical barrier effect, which led to higher thermal stability. Meanwhile, the gross calorific values of the SDS-LDH/SA were reduced compared to that of the pure SA, as an indication of lowering the thermal hazard of SA. The research results indicate that the SDS-LDH effectively improves the thermal safety of SA, providing an engineering example to develop more favorable SA materials for applications in the field of thermal insulation.

Acknowledgements This work is supported by the National Natural Science Foundation of China (Nos. 52274248 and 51904336). This work was also supported in part by the High Performance Computing Center of Central South University.

Author contributions Writing—original draft: Min Hu and Zhi Li; Writing—review and editing: Xiaoxu Wu, Fang Zhou, Xudong Cheng, Qiong Liu, Zhenkui Chen and Zhi Li; Visualization: Min Hu and Kai Shen; Investigation: Min Hu; Supervision and funding acquisition: Zhi Li. All authors have read and agreed to the published version of the manuscript.

Compliance with ethical standards

Conflict of interest The authors declare no competing interests.

References

- Liu Z, Lyu J, Fang D, Zhang X (2019) Nanofibrous kevlar aerogel threads for thermal insulation in harsh environments. *ACS Nano* 13(5):5703–5711. <https://doi.org/10.1021/acsnano.9b01094>
- Tao J, Yang F, Wu T, Shi J, Zhao H-B, Rao W (2023) Thermal insulation, flame retardancy, smoke suppression, and reinforcement of rigid polyurethane foam enabled by incorporating a P/Cu-hybrid silica aerogel. *Chem Eng J* 461:142061. <https://doi.org/10.1016/j.cej.2023.142061>
- Tang R, Hong W, Srinivasakannan C, Liu X, Wang X, Duan X (2022) A novel mesoporous Fe-silica aerogel composite with phenomenal adsorption capacity for malachite green. *Sep Purif Technol* 281:119950. <https://doi.org/10.1016/j.seppur.2021.119950>
- Liu Y, Zheng P, Wu H, Zhang Y (2023) Preparation and dynamic moisture adsorption of fiber felt/silica aerogel composites with ultra-low moisture adsorption rate. *Constr Build Mater* 363:129825. <https://doi.org/10.1016/j.conbuildmat.2022.129825>
- Zhou W, Fu W, Lv G, Liu J, Peng H, Fang T, Tan X, Chen Z (2023) Preparation and properties of CaCl₂·6H₂O/silica aerogel composite phase change material for building energy conservation. *J Mol Liq* 382:121986. <https://doi.org/10.1016/j.molliq.2023.121986>
- Ma L, Luo D, Hu H, Li Q, Yang R, Zhang S, Li D (2023) Energy performance of a rural residential building with PCM-silica aerogel sunspace in severe cold regions. *Energy Build* 280:112719. <https://doi.org/10.1016/j.enbuild.2022.112719>
- Li Z, Zhao S, Koebel MM, Malfait WJ (2020) Silica aerogels with tailored chemical functionality. *Mater Des* 193:108833. <https://doi.org/10.1016/j.matdes.2020.108833>
- Li Z, Cheng X, Shi L, He S, Gong L, Li C, Zhang H (2016) Flammability and oxidation kinetics of hydrophobic silica aerogels. *J Hazard Mater* 320:350–358. <https://doi.org/10.1016/j.jhazmat.2016.07.054>
- Li Z, Wang Y, Wu X, Liu Q, Li M, Shi L, Cheng X (2023) Surface chemistry, skeleton structure and thermal safety of methylsilyl modified silica aerogels by heat treatment in an argon atmosphere. *J Non-Cryst Solids* 611:122335. <https://doi.org/10.1016/j.jnoncrysol.2023.122335>
- Li Z, Huang S, Shi L, Li Z, Liu Q, Li M (2019) Reducing the flammability of hydrophobic silica aerogels by doping with hydroxides. *J Hazard Mater* 373:536–546. <https://doi.org/10.1016/j.jhazmat.2019.03.112>
- Zhang Y, Wu L, Deng X, Deng Y, Wu X, Shi L, Li M, Liu Q, Cheng X, Li Z (2021) Improving the flame retardance of hydrophobic silica aerogels through a facile post-doping of magnesium hydroxide. *Adv Powder Technol* 32(6):1891–1901. <https://doi.org/10.1016/j.apt.2021.03.041>
- Sun M, Wang Y, Wang X, Liu Q, Li M, Shulga YM, Li Z (2022) In-situ synthesis of layered double hydroxide/silica aerogel composite and its thermal safety characteristics. *Gels* 8(9):581. <https://doi.org/10.3390/gels8090581>
- Xue T, Fan W, Zhang X, Zhao X, Yang F, Liu T (2021) Layered double hydroxide/graphene oxide synergistically enhanced polyimide aerogels for thermal insulation and fire-retardancy. *Compos Part B Eng* 219:108963. <https://doi.org/10.1016/j.compositesb.2021.108963>
- Zheng Z, Zhao Y, Hu J, Wang H (2020) Flexible, strong, multi-functional graphene oxide/silica-based composite aerogels via a double-cross-linked network approach. *ACS Appl Mater Interfaces* 12(42):47854–47864. <https://doi.org/10.1021/acsami.0c14333>
- Li Z, Hu M, Shen K, Liu Q, Li M, Chen Z, Cheng X, Wu X (2024) Tuning thermal stability and fire hazards of hydrophobic silica aerogels via doping reduced graphene oxide. *J Non-Cryst Solids* 625:122747. <https://doi.org/10.1016/j.jnoncrysol.2023.122747>
- Yang K, Liu W, Zhang S, Yu W, Shi J, Lin Z, Zheng Q (2022) Influence of the aggregated structures of layered double hydroxide nanoparticles on the degradation behavior of poly(butylene adipate-co-terephthalate) composites. *Appl Clay Sci* 230:106713. <https://doi.org/10.1016/j.clay.2022.106713>
- Marcu I-C, Pavel OD (2022) Layered double hydroxide-based catalytic materials for sustainable processes. *Catalysts* 12(8):816. <https://doi.org/10.3390/catal12080816>
- Sohrabnezhad S, Poursafar Z, Asadollahi A (2020) Synthesis of novel core@shell of MgAl layered double hydroxide @ porous magnetic shell (MgAl-LDH@PMN) as carrier for ciprofloxacin drug. *Appl Clay Sci* 190:105586. <https://doi.org/10.1016/j.clay.2020.105586>

19. Zheng W, Yu J, Hu Z, Ruan X, Li X, Dai Y, He G (2022) 3D hollow CoNi-LDH nanocages based MMMs with low resistance and CO₂-philic transport channel to boost CO₂ capture. *J Membr Sci* 653:120542. <https://doi.org/10.1016/j.memsci.2022.120542>
20. Ahmed MA, Mohamed AA (2023) A systematic review of layered double hydroxide-based materials for environmental remediation of heavy metals and dye pollutants. *Inorg Chem Commun* 148:110325. <https://doi.org/10.1016/j.inoche.2022.110325>
21. Deng C, Liu Y, Jian H, Liang Y, Wen M, Shi J, Park H (2023) Study on the preparation of flame retardant plywood by intercalation of phosphorus and nitrogen flame retardants modified with Mg/Al-LDH. *Constr Build Mater* 374:130939. <https://doi.org/10.1016/j.conbuildmat.2023.130939>
22. Karami Z, Jouyandeh M, Hamad SM, Ganjali MR, Aghazadeh M, Torre L, Puglia D, Saeb MR (2019) Curing epoxy with Mg–Al LDH nanoplatelets intercalated with carbonate ion. *Prog Org Coat* 136:105278. <https://doi.org/10.1016/j.porgcoat.2019.105278>
23. Cai J, Heng H-M, Hu X-P, Xu Q-K, Miao F (2016) A facile method for the preparation of novel fire-retardant layered double hydroxide and its application as nanofiller in UP. *Polym Degrad Stab* 126:47–57. <https://doi.org/10.1016/j.polymdegradstab.2016.01.013>
24. Kalali EN, Wang X, Wang D-Y (2016) Multifunctional intercalation in layered double hydroxide: toward multifunctional nanohybrids for epoxy resin. *J Mater Chem A* 4(6):2147–2157. <https://doi.org/10.1039/C5TA09482H>
25. Ye L, Ding P, Zhang M, Qu B (2008) Synergistic effects of exfoliated LDH with some halogen-free flame retardants in LDPE/EVA/HFMH/LDH nanocomposites. *J Appl Polym Sci* 107(6):3694–3701. <https://doi.org/10.1002/app.27526>
26. Zhang S, Yan Y, Wang W, Gu X, Li H, Li J, Sun J (2018) Intercalation of phosphotungstic acid into layered double hydroxides by reconstruction method and its application in intumescent flame retardant poly (lactic acid) composites. *Polym Degrad Stab* 147:142–150. <https://doi.org/10.1016/j.polymdegradstab.2017.12.004>
27. Xu S, Zhang M, Li S-Y, Zeng H-Y, Tian X-Y, Wu K, Hu J, Chen C-R, Pan Y (2020) Intercalation of a novel containing nitrogen and sulfur anion into hydrotalcite and its highly efficient flame retardant performance for polypropylene. *Appl Clay Sci* 191:105600. <https://doi.org/10.1016/j.clay.2020.105600>
28. Du J-Z, Jin L, Zeng H-Y, Feng B, Xu S, Zhou E-G, Shi X-K, Liu L, Hu X (2019) Facile preparation of an efficient flame retardant and its application in ethylene vinyl acetate. *Appl Clay Sci* 168:96–105. <https://doi.org/10.1016/j.clay.2018.11.004>
29. Wu K, Xu S, Tian X-Y, Zeng H-Y, Hu J, Guo Y-H, Jian J (2021) Renewable lignin-based surfactant modified layered double hydroxide and its application in polypropylene as flame retardant and smoke suppression. *Int J Biol Macromol* 178:580–590. <https://doi.org/10.1016/j.ijbiomac.2021.02.148>
30. Jiang Y, Gu X, Zhang S, Tang W, Zhao J (2015) The preparation and characterization of sulfamic acid-intercalated layered double hydroxide. *Mater Lett* 150:31–34. <https://doi.org/10.1016/j.matlet.2014.12.096>
31. Shen H, Wu W, Wang Z, Wu W, Yuan Y, Feng Y (2021) Effect of modified layered double hydroxide on the flammability of intumescent flame retardant PP nanocomposites. *J Appl Polym Sci* 138(40):51187. <https://doi.org/10.1002/app.51187>
32. Chuang YH, Tzou YM, Wang MK, Liu CH, Chiang PN (2008) Removal of 2-chlorophenol from aqueous solution by Mg/Al layered double hydroxide (LDH) and modified LDH. *Ind Eng Chem Res* 47(11):3813–3819. <https://doi.org/10.1021/ie071508e>
33. Liu Y, Yu Z, Wang Q, Zhu X, Long R, Li X (2021) Application of sodium dodecyl sulfate intercalated CoAl LDH composite materials (RGO/PDA/SDS-LDH) in membrane separation. *Appl Clay Sci* 209:106138. <https://doi.org/10.1016/j.clay.2021.106138>
34. Zhang P, Wang T, Qian G, Wu D, Frost RL (2015) Effective intercalation of sodium dodecylsulfate (SDS) into hydrocalumite: mechanism discussion via near-infrared and mid-infrared investigations. *Spectrochim Acta A Mol Biomol Spectrosc* 149:166–172. <https://doi.org/10.1016/j.saa.2015.04.012>
35. Brunauer S, Emmett PH, Teller E (1938) Adsorption of gases in multimolecular layers. *J Am Chem Soc* 60(2):309–319. <https://doi.org/10.1021/ja01269a023>
36. Barrett EP, Joyner LG, Halenda PP (1951) The determination of pore volume and area distributions in porous substances. I. Computations from nitrogen isotherms. *J Am Chem Soc* 73(1):373–380. <https://doi.org/10.1021/ja01145a126>
37. Huang S, Wu X, Li Z, Shi L, Zhang Y, Liu Q (2020) Rapid synthesis and characterization of monolithic ambient pressure dried MTMS aerogels in pure water. *J Porous Mater* 27(4):1241–1251. <https://doi.org/10.1007/s10934-020-00902-3>
38. Li L, Jiang K, Qian Y, Han H, Qiao P, Zhang H (2020) Effect of organically intercalation modified layered double hydroxides-graphene oxide hybrids on flame retardancy of thermoplastic polyurethane nanocomposites. *J Therm Anal Calorim* 142(2):723–733. <https://doi.org/10.1007/s10973-020-09263-0>
39. Ravuru SS, Jana A, De S (2019) Synthesis of NiAl-layered double hydroxide with nitrate intercalation: application in cyanide removal from steel industry effluent. *J Hazard Mater* 373:791–800. <https://doi.org/10.1016/j.jhazmat.2019.03.122>
40. Deng L, Zeng H, Shi Z, Zhang W, Luo J (2018) Sodium dodecyl sulfate intercalated and acrylamide anchored layered double hydroxides: a multifunctional adsorbent for highly efficient removal of congo red. *J Colloid Interface Sci* 521:172–182. <https://doi.org/10.1016/j.jcis.2018.03.040>
41. Zheng Y, Chen Y (2017) Preparation of polypropylene/Mg–Al layered double hydroxides nanocomposites through wet pan-milling: formation of a second-staging structure in LDHs intercalates. *RSC Adv* 7(3):1520–1530. <https://doi.org/10.1039/C6RA26050K>
42. Zhang P, Qian G, Xu ZP, Shi H, Ruan X, Yang J, Frost RL (2012) Effective adsorption of sodium dodecylsulfate (SDS) by hydrocalumite (CaAl-LDH-Cl) induced by self-dissolution and reprecipitation mechanism. *J Colloid Interface Sci* 367(1):264–271. <https://doi.org/10.1016/j.jcis.2011.10.036>
43. Zhang LH, Li F, Evans DG, Duan X (2010) Evolution of structure and performance of Cu-based layered double hydroxides. *J Mater Sci* 45(14):3741–3751. <https://doi.org/10.1007/s10853-010-4423-6>
44. Xie J, Wang Z, Zhao Q, Yang Y, Xu J, Waterhouse G. I. N, Zhang K, Li S, Jin P, Jin G (2018) Scale-Up Fabrication of Biodegradable Poly (Butylene Adipate-Co-Terephthalate)/Organophilic-Clay Nanocomposite Films for Potential Packaging Applications. *ACS Omega* 3:1187–1196. <https://doi.org/10.1021/acsomega.7b02062>
45. Basu D, Das A, Stoeckelhuber KW, Wagenknecht U, Heinrich G (2014) Advances in layered double hydroxide (LDH)-based elastomer composites. *Prog Polym Sci* 39(3):594–626. <https://doi.org/10.1016/j.progpolymsci.2013.07.011>
46. Yadollahi M, Namazi H, Barkhordari S (2014) Preparation and properties of carboxymethyl cellulose/layered double hydroxide bionanocomposite films. *Carbohydr Polym* 108:83–90. <https://doi.org/10.1016/j.carbpol.2014.03.024>
47. Nagendra B, Rosely C, Leuteritz A, Reuter U, Gowd EB (2017) Polypropylene/layered double hydroxide nanocomposites: influence of LDH intralayer metal constituents on the properties of polypropylene. *ACS Omega* 2(1):20–31
48. Li L, Qian Y, Han H, Qiao P, Zhang H (2021) Effects of functional intercalation and surface modification on the flame retardant performance of EVA/LDHs composites. *Polym Polym Compos* 29(7):842–853. <https://doi.org/10.1177/0967391120938174>
49. Wang Y, Yuan Z, Zhang Z, Xin Y, Fujita T, Wei Y (2022) In situ one-step fabrication of superhydrophobic layered double hydroxide on Al alloys for anti-corrosion. *Appl Surf Sci* 593:153400. <https://doi.org/10.1016/j.apsusc.2022.153400>

50. Xu K, Chen G, Shen J (2013) Exfoliation and dispersion of micrometer-sized LDH particles in poly(ethylene terephthalate) and their nanocomposite thermal stability. *Appl Clay Sci* 75–76(5):114–119
51. Zhao J, Fu X, Zhang S, Hou W (2011) Water dispersible avermectin-layered double hydroxide nanocomposites modified with sodium dodecyl sulfate. *Appl Clay Sci* 51(4):460–466
52. Rojas F, Kornhauser I, Felipe C, Esparza JM, Cordero S, Domínguez A, Riccardo JL (2002) Capillary condensation in heterogeneous mesoporous networks consisting of variable connectivity and pore-size correlation. *Phys Chem Chem Phys* 4(11):2346–2355
53. Al-Oweini R, El-Rassy H (2009) Synthesis and characterization by FTIR spectroscopy of silica aerogels prepared using several Si(OR)₄ and RⁿSi(OR)₃ precursors. *J Mol Struct* 919(1–3):140–145
54. Shi G, He S, Chen G, Ruan C, Ma Y, Chen Q, Jin X, Liu X, He C, Du C, Dai H, Yang X (2022) Crayfish shell-based micro-mesoporous activated carbon: insight into preparation and gaseous benzene adsorption mechanism. *Chem Eng J* 428:131148. <https://doi.org/10.1016/j.cej.2021.131148>
55. Li Z, Zhang Y, Huang S, Wu X, Shi L, Liu Q (2020) Thermal stability and pyrolysis characteristics of MTMS aerogels prepared in pure water. *J Nanopart Res* 22(10):334. <https://doi.org/10.1007/s11051-020-05062-8>
56. Bhagat S, Rao A (2006) Surface chemical modification of TEOS based silica aerogels synthesized by two step (acid–base) sol–gel process. *Appl Surf Sci* 252(12):4289–4297
57. Zhang W, Li Z, Shi L, Li Z, Luo Y, Liu Q, Huang R (2019) Methyltrichlorosilane modified hydrophobic silica aerogels and their kinetic and thermodynamic behaviors. *J Sol Gel Sci Technol* 89(2):448–457. <https://doi.org/10.1007/s10971-018-4882-9>
58. Li Zhi, Cheng X, He S, Shi X, Yang H (2015) Characteristics of ambient-pressure-dried aerogels synthesized via different surface modification methods. *J Sol Gel Sci Technol* 76(1):138–149. <https://doi.org/10.1007/s10971-015-3760-y>
59. Babakhani S, Talib ZA, Hussein MZ, Ahmed AAA (2014) Optical and thermal properties of Zn/Al-layered double hydroxide nanocomposite intercalated with sodium dodecyl sulfate. *J Spectrosc* 2014:1–10. <https://doi.org/10.1155/2014/467064>
60. Li X-Z, Liu S-R, Guo Y (2016) Polyaniline-intercalated layered double hydroxides: synthesis and properties for humidity sensing. *RSC Adv* 6(68):63099–63106. <https://doi.org/10.1039/C6RA10093G>
61. Lv F, Wu Y, Zhang Y, Shang J, Chu PK (2012) Structure and magnetic properties of soft organic ZnAl-LDH/polyimide electromagnetic shielding composites. *J Mater Sci* 47(4):2033–2039
62. Costa FR, Leuteritz A, Wagenknecht U, Jehnichen D, Häußler L, Heinrich G (2008) Intercalation of Mg–Al layered double hydroxide by anionic surfactants: preparation and characterization. *Appl Clay Sci* 38(3–4):153–164. <https://doi.org/10.1016/j.clay.2007.03.006>
63. Costa FR, Leuteritz A, Wagenknecht U, Landwehr M, Jehnichen D, Haeussler L, Heinrich G (2009) Alkyl sulfonate modified LDH: effect of alkyl chain length on intercalation behavior, particle morphology and thermal stability. *Appl Clay Sci* 44(1–2):7–14
64. Zhang P, Shi H, Xiuxiu R, Guangren Q, Frost RL (2011) N-dodecylsulfate modification of hydrocalumite and subsequent effect on the structure and thermal decomposition. *J Therm Anal Calorim* 104(2):743–747. <https://doi.org/10.1007/s10973-010-1001-8>
65. Tao Q, Yuan J, Frost RL, He H, Yuan P, Zhu J (2009) Effect of surfactant concentration on the stacking modes of organo-silylated layered double hydroxides. *Appl Clay Sci* 45(4):262–269. <https://doi.org/10.1016/j.clay.2009.06.007>
66. Kantor Z, Wu T, Zeng Z, Gaan S, Lehner S, Jovic M, Bonnin A, Pan Z, Mazrouei-Sebdani Z, Opris DM, Koebel MM, Malfait WJ, Zhao S (2022) Heterogeneous silica-polyimide aerogel-in-aerogel nanocomposites. *Chem Eng J* 443:136401. <https://doi.org/10.1016/j.cej.2022.136401>
67. Ji S, Chen Y, Wang X, Zhang Z, Wang D, Li Y (2020) Chemical synthesis of single atomic site catalysts. *Chem Rev* 120(21):11900–11955. <https://doi.org/10.1021/acs.chemrev.9b00818>

Publisher's note Springer Nature remains neutral with regard to jurisdictional claims in published maps and institutional affiliations.

Springer Nature or its licensor (e.g. a society or other partner) holds exclusive rights to this article under a publishing agreement with the author(s) or other rightsholder(s); author self-archiving of the accepted manuscript version of this article is solely governed by the terms of such publishing agreement and applicable law.